JM PAPERS

Particle chirality does not matter in the large-scale features of strong turbulence

G. Piumini[1],†, M.P.A. Assen[1], D. Lohse[1,2] and R. Verzicco[1,3,4],†

[1]Physics of Fluids Group and Max Planck Center for Complex Fluid Dynamics, Department of Science and Technology, J.M. Burgers Center for Fluid Dynamics, and MESA+ Institute, University of Twente, P.O. Box 217, 7500AE Enschede, The Netherlands

[2]Max Planck Institute for Dynamics and Self-Organization, Am Fassberg 17, 37077 Göttingen, Germany

[3]Dipartimento di Ingegneria Industriale, University of Rome 'Tor Vergata', Via del Politecnico 1, 00133 Roma, Italy

[4]Gran Sasso Science Institute, Viale F. Crispi 7, 67100 L'Aquila, Italy

We use three-dimensional direct numerical simulations of homogeneous isotropic turbulence in a cubic domain to investigate the dynamics of heavy, chiral, finite-size inertial particles and their effects on the flow. Using an immersed-boundary method and a complex collision model, four-way coupled simulations have been performed, and the effects of particle-to-fluid density ratio, turbulence strength and particle volume fraction have been analysed. We find that freely falling particles on the one hand add energy to the turbulent flow but, on the other hand, they also enhance the flow dissipation: depending on the combination of flow parameters, the former or the latter mechanism prevails, thus yielding enhanced or weakened turbulence. Furthermore, particle chirality entails a preferential angular velocity which induces a net vorticity in the fluid phase. As turbulence strengthens, the energy introduced by the falling particles becomes less relevant and stronger velocity fluctuations alter the solid phase dynamics, making the effect of chirality irrelevant for the large-scale features of the flow. Moreover, comparing the time history of collision events for chiral particles and spheres (at the same volume fraction) suggests that the former tend to entangle, in contrast to the latter which rebound impulsively.

† Email addresses for correspondence: g.piumini@utwente.nl, verzicco@uniroma2.it

1. Introduction

Turbulent, inertial particle-laden flows are ubiquitous in natural and engineering environments (Balmforth & Provenzale 2001). Aerosols in clouds (Shaw 2003), particle-driven gravity currents (Necker *et al.* 2005), sediments in oceans or rivers (Hargrave 1985), sand storms in the atmosphere (Voilland 2018) as well as fluidisation of pipe or open-channel flows in industrial processes (Lashgari *et al.* 2014) are just a few examples among many. Owing to the high practical interest, investigation of these problems has increased in the last decade, especially thanks to the massive improvements achieved in terms of measurement and simulation performance. There are many aspects that make this topic an extraordinary challenge: the different properties of both particles and the carrier fluid, the multi-way coupling between continuous and dispersed phases, and the relevant difference in spatial and time scales (Toschi & Bodenschatz 2009; Brandt & Coletti 2022). The interaction between the two phases can affect the flow both at large and small scales depending on factors such as particle shape, size and volume/mass fraction. Depending on their relative size to the viscous scale, heavy particles can attenuate or enhance turbulence (Yu *et al.* 2021), in contrast to small, settling particles which always lead to turbulence damping (Zhao, Andersson & Gillissen 2010). Moreover, particles of greater mass density than the surrounding fluid can detach from the flow, leading to preferential sampling, small-scale fractal clustering and significant relative velocities (Bec, Gustavsson & Mehlig 2024).

In recent years, studies have predominantly focused on particles with vanishing inertia (behaving as passive tracers) or highly symmetric shapes such as spheres or ellipsoids (Shaw 2003; Voilland 2018; Sozza *et al.* 2022). However, investigations into anisotropic particles have gained traction only recently. Elastic fibres, for instance, induce similar turbulence damping as spheres but can also modify the energy scale-by-scale distribution (Dotto & Marchioli 2019; Di Giusto & Marchioli 2022; Olivieri, Cannon & Rosti 2022). Inertial rods also possess the potential to influence turbulence-regeneration mechanisms, with rigid, inertia-less fibres generating additional stresses that dampen counter-rotating vortices in the wall region, leading to drag reduction. Inertial fibres may preferentially segregate into low-speed streaks, thereby delaying fluid flow (Voth & Soldati 2017).

Despite the abundance of literature in this field, most studies have focused on isotropic or highly symmetric particle shapes (Brandt & Coletti 2022), overlooking a significant portion of the parameter space concerning strongly asymmetric large particles in turbulence (Voth & Soldati 2017). The present paper is a first attempt aimed at filling this gap. Among several possibilities, we have considered chiral particles which are distinct from their mirror image (Roos & Roos 2015). We have chosen chiral particles because they break spatial reflection symmetry and couple translational and rotational degrees of freedom. A particle forced to translate in a fluid will also rotate and *vice versa*; this feature is also present in nature and can be appreciated by watching the falling of maple seeds. Indeed, there are multiple examples of chiral objects in nature and technology. Most of flagella of bacteria and micro-organisms are chiral, but also propellers and impellers in mixers and industrial plants. Chan *et al.* (2024) provides evidence that in nature there are more chiral objects than non-chiral ones. We wish to point out however that our study is not focused on applications but rather on the effect of chiral objects on homogenous isotropic turbulence.

Questions we ask are as follows. How do chiral particles behave in a turbulent flow? Are they able to modify some features of turbulence? What is the influence of parameters like solid-to-fluid density ratio, turbulence strength and solid phase volume fraction?

The paper is organised as follows. In § 2, we outline the numerical model and the set-up of the simulations. The findings are discussed in § 3, and the complex interplay between particle and flow dynamics is illustrated by taking into account the effect of multiple parameters separately. Closing remarks and an outlook are given in § 4. The paper is completed with additional material in Appendices A–C.

2. Problem and methods

2.1. *Set-up*

We consider a three-periodic cubic domain filled with a Newtonian fluid of density ρ_f laden by N_p identical chiral particles of density ρ_p. Each particle is made of three perpendicular cylinders, arranged as in figure 1(a), with the ends rounded by spherical caps. Let V_p be the volume of the particle and D_{eq} the diameter of the equivalent sphere (volume wise) which is assumed as unit length throughout the paper. The particle can be then enclosed in a cubic bounding box of edges $\ell_x = \ell_y = \ell_z = 1.5D_{eq}$ while the diameter of the cylindrical legs is $d \simeq 0.42D_{eq}$. The particle is convex, as its centroid falls outside its volume, with coordinates $G = (0.75, 0.42, 1.08)$ in D_{eq} units measured from the origin O. The asymmetric shape implies principal axes not aligned with any particle legs yielding for their unit vectors $\hat{x}_p = (-0.774, 0.447, 0.447)$, $\hat{y}_p = (0.000, -0.707, 0.707)$ and $\hat{z}_p = (-0.633, -0.548, -0.548)$, and for the principal moments of inertia $I_{xp} = 0.076$, $I_{yp} = 0.226$ and $I_{zp} = 0.248$ in $\rho_p D_{eq}^5$ units. It is worthwhile pointing out that the present particles are equivalent to a sphere of diameter D_{eq} only volume wise; in fact, the wetted surface of the former is approximately 50 % bigger than the equivalent sphere while the encumbrance of the bounding box is ≈ 3.4 times that of a cube enclosing the sphere. These differences are relevant for the particle/particle and particle/fluid interaction as will be discussed in § 3.

The flow domain is cubic with edges of length $L_x = L_y = L_z = 10D_{eq}$ in each direction and a constant gravitational acceleration $\boldsymbol{g}$ anti-parallel to the z direction. Particles are initially distributed randomly, both in position and orientation, within the computational domain, the only constraint being that they cannot intersect spatially: a schematic of the system is shown in figure 1(b).

After an initial transient, the system attains a statistical steady state over which data are collected for the analysis; depending on the problem parameters, statistic convergence is achieved for different time windows. We define the large-eddy-turnover time $T_e = u_{rms}^2/\varepsilon$ with the velocity fluctuations u_{rms} and the kinetic energy dissipation rate ε of the turbulent flow, and the 'observation time' T_o the integration time window (in D_{eq}/U units, U being the flow velocity scale): simulations of homogeneous isotropic turbulence (HIT) without particles have been run for $33 \leq T_o/T_e \leq 10^3$, while for the simulations with a single particle, we had $510 \leq T_o/T_e \leq 860$. Finally, the cases with $N_p = 20$ particles have been integrated for $75 \leq T_o/T_e \leq 840$. For each simulation, the duration of the integration has been decided by monitoring the quantities of interest and verifying that their values did not change appreciably during the final part of the simulation.

Before concluding this section, we wish to point out that in some studies dealing with settling particles in turbulence (see for example Chouippe & Uhlmann 2015), an elongated domain in the direction of gravity has been employed to avoid possible correlation effects produced by the preferential velocity direction. In this study, we have preliminarily verified that, at least for the flow quantities considered in the present analysis, the differences in
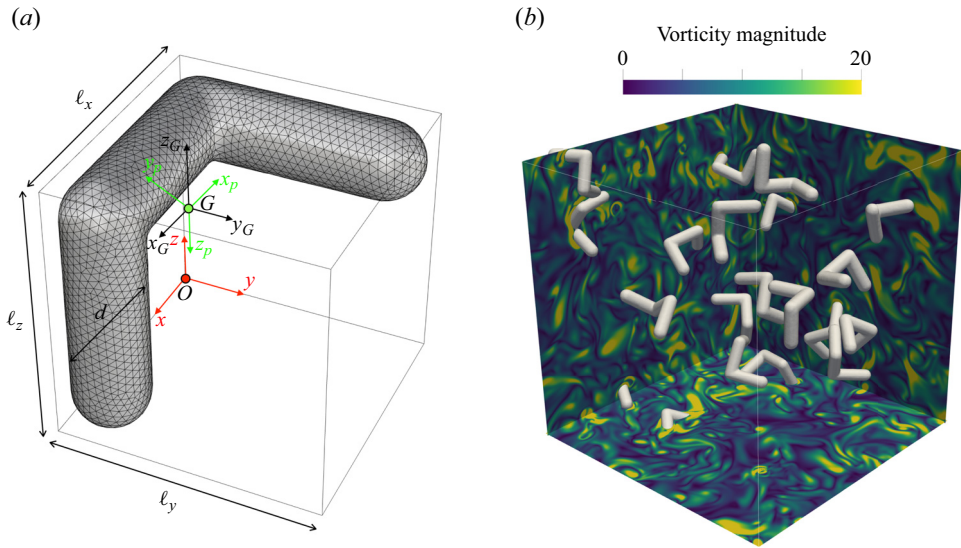
G. Piumini, M.P.A. Assen, D. Lohse and R. Verzicco

(*a*)

(*b*)

Figure 1. (*a*) Representation of a chiral particle with global (red), body centroid (black) and principal inertia (green) reference frames. The green bullet (G) outside the particle is its centre of mass. (*b*) Perspective view of the system with randomly distributed particles in homogeneous isotropic turbulence for $Re_\lambda = 75$, volume fraction $\phi = 1\,\%$ and density ratio $\rho_p/\rho_f = 2$. Colours of the background are non-dimensional vorticity magnitude contours ranging from 0 (blue) to 20 (yellow).

the results obtained in a cubic and in an elongated domain are negligible; selected results from these tests are given in Appendix C.

2.2. *Carrier phase*

The governing relations for the fluid phase are the incompressible Navier–Stokes equations and the continuity equation which, in non-dimensional form, read

$$\frac{\partial \boldsymbol{u}}{\partial t} + (\boldsymbol{u} \cdot \boldsymbol{\nabla})\boldsymbol{u} = -\boldsymbol{\nabla}p + \frac{1}{Re}\nabla^2 \boldsymbol{u} + \mathbf{f}, \quad \boldsymbol{\nabla} \cdot \boldsymbol{u} = 0. \tag{2.1a,b}$$

Here, $\boldsymbol{u}$ and p are fluid velocity vector and kinematic pressure, respectively, while $Re = D_{eq}U/\nu$ is the Reynolds number based on the length D_{eq} and the flow velocity U scales. The last term in the first of (2.1a,b) is a vector containing two volume forces $\mathbf{f} = \boldsymbol{f}_T + \boldsymbol{f}_P$: $\boldsymbol{f}_T$ sustains the HIT flow while $\boldsymbol{f}_P$ is the immersed boundary method (IBM) forcing which accounts for the presence of solid particles and allows for the two-way coupling between solid and fluid phases.

We numerically solve the governing equations (2.1a,b) with our in-house advanced finite-difference code ('AFiD'), which is extensively described and validated in van der Poel *et al.* (2015) and Spandan *et al.* (2020). The main features are: spatial derivatives are approximated by conservative, second-order accurate finite-differences discretised on a staggered mesh which is uniform and homogeneous ($\Delta x = \Delta y = \Delta z = \Delta$). A combination of Crank–Nicolson and low-storage third-order Runge–Kutta schemes is used to integrate the viscous terms implicitly and all other terms explicitly. Finally, pressure and momentum are strongly coupled through a fractional-step method as described by Rai & Moin (1991) and Verzicco & Orlandi (1996).

RUN	T_L	σ	Re_λ	K	ε	λ/D_{eq}	η/Δ	N^3
Re15	5.0×10^{-1}	1.7×10^{-2}	13.0	8.4×10^{-3}	2.7×10^{-4}	1.74	6.30	256^3
Re30	8.5×10^{-1}	6.2×10^{-3}	33.9	1.1×10^{-1}	7.5×10^{-3}	1.22	2.75	256^3
Re60	8.5×10^{-1}	4.4×10^{-1}	66.7	1.3×10^{0}	2.4×10^{-1}	0.72	2.31	512^3
Re80	8.2×10^{-2}	2.6×10^{0}	78.5	2.2×10^{0}	5.3×10^{-1}	0.64	1.90	512^3
Re140	8.5×10^{-2}	8.3×10^{0}	134.0	1.7×10^{1}	1.0×10^{1}	0.40	1.83	1024^3

Table 1. Run parameters of the single-phase simulations: $\lambda = (15\nu u_{rms}^2/\varepsilon)^{1/2}$ is the Taylor microscale while Re_λ is the corresponding Reynolds number, $\eta = (\nu^3/\varepsilon)^{1/4}$ the Kolmogorov length scale, $N = N_x = N_y = N_z$ is the number of gridpoints of the Eulerian mesh in each direction, K is the kinetic energy, and T_L and σ are the input parameters for the HIT forcing.

2.3. *Homogeneous isotropic turbulence forcing method*

The HIT forcing f_T is prescribed, similarly to Chouippe & Uhlmann (2015), adopting the method introduced by Eswaran & Pope (1988). It allows to attain a statistically stationary velocity field by forcing large scale (small wavenumber) components. This is achieved through a random Uhlenbeck–Ornstein process via a vector $\hat{b}(k, t)$ whose components are prescribed in time according to

$$\hat{b}_i(k, t + \Delta t) = \hat{b}_i(k, t)\left(1 - \frac{\Delta t}{T_L}\right) + e_i(k, t)\left(2\sigma^2\frac{\Delta t}{T_L}\right)^{1/2}, \quad i = 1, 2, 3. \qquad (2.2)$$

Here, $k = (l, m, n)$ is the wavenumber vector, Δt the numerical integration time step and $e_i(k, t)$ a complex random number drawn from a standardised Gaussian distribution, and T_L and σ^2 are time scale and variance of the random process.

The forcing term $\hat{f}_T(k, t)$, in Fourier space, is non-zero only in the band $|k| \leq k_f = 2.3$ and the final forcing is obtained by an orthogonal projection of $\hat{b}(k, t)$:

$$\hat{f}_T(k, t) = \hat{b}(k, t) - k(k \cdot \hat{b}(k, t + \Delta t))/(k \cdot k), \qquad (2.3)$$

which is needed to ensure the divergence-free condition. More details about the HIT forcing can be found from Eswaran & Pope (1988) and Chouippe & Uhlmann (2015).

Note that (2.3) defines the forcing in Fourier space while (2.1*a,b*) are solved in the physical space. Therefore, the former expression must be transformed into values to be prescribed at the Eulerian grid points. To determine the field in physical space $f_T(x, t)$, we compute the Fourier coefficients from (2.3), with $\hat{f}_{lmn}(t) = \hat{f}(l, m, n, t)$, from which the value at the discrete position $x_{i,j,k} = (i\Delta, j\Delta, k\Delta)$ is obtained by

$$f_T(x_{ijk}, t) = \sum_{l=-N_f}^{N_f} \sum_{m=-N_f}^{N_f} \sum_{n=-N_f}^{N_f} \hat{f}_{lmn}(t) \exp(\jmath k \cdot x_{i,j,k}) \quad \forall\, i, j, k, \qquad (2.4)$$

where $N_f^3 = 27$ is the number of forced wavenumbers and $\jmath$ the imaginary unit.

The HIT forcing and additional simulation parameters are reported in table 1 where it is also shown that the spatial resolution is always smaller than the Kolmogorov scale.
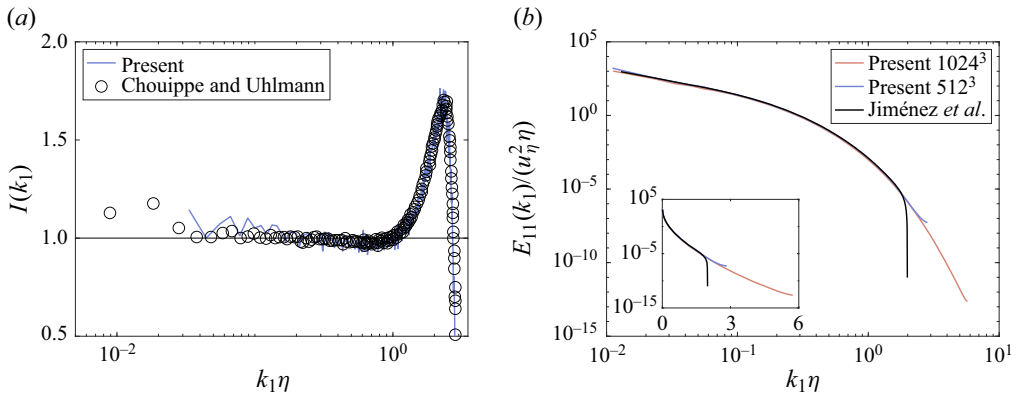
Figure 2. Single-phase HIT at $Re_\lambda = 140$: (*a*) isotropy parameter *I*, as defined in (2.5), compared with Chouippe & Uhlmann (2015). (*b*) One-dimensional energy spectrum, compared with Jiménez *et al.* (1993).

A validation of the flow solver is provided by computing the one-dimensional longitudinal energy spectrum $E_{11}(k_1)$ and the isotropy parameter:

$$I(k_1) = \frac{E_{11}(k_1) - k_1 \partial E_{11}(k_1)/\partial k_1}{2E_{22}(k_1)} \tag{2.5}$$

for a case at $Re_\lambda \approx 140$, the latter being the Reynolds number based on the Taylor microscale $\lambda = (15\nu u_{rms}^2)^{1/2}$ and on the root-mean-squared (r.m.s.) value of the velocity fluctuations u_{rms}.

The comparison with the data by Jiménez *et al.* (1993) and Chouippe & Uhlmann (2015) is given in figure 2, showing a very good agreement for both quantities.

As an aside, we note that results obtained with a resolution 512^3 ($\eta/\Delta = 0.92$) and 1024^3 ($\eta/\Delta = 1.83$) perfectly agree and, in both cases, the viscous range shows an exponential decay, evidenced by the linear slope when plotted in semi-log axes (Jiménez *et al.* 1993). The reason for the sharp decay of the benchmark data in the viscous range is that they had been obtained using the spectral code developed by Rogallo (1981), which is very strict on isotropy. In fact, to approximate the flow as isotropically as possible, it applies every time step a mask in *k*-space, such that the energy outside the sphere $|k\eta| = 2$ is set to zero (J. Jiménez, *Personal Communication*).

2.4. *Immersed boundary method*

As mentioned above, the term **f** on the right-hand side of the first equation (2.1*a*,*b*) contains also the IBM part f_P which allows for two-way coupling between particles and fluid. Here we have employed the method proposed by de Tullio & Pascazio (2016) in combination with the regularised Dirac delta function of Roma, Peskin & Berger (1999). The surface of each solid object is discretised by N_l equilateral triangular elements (see figure 1*a*) and Lagrangian markers are placed at their centroids. The IBM forcing term is computed on these Lagrangian markers, to satisfy velocity boundary conditions, and then transferred back to the Eulerian mesh to impose the effect of the solid phase on the flow. To avoid unforced Eulerian nodes, which would result in surface 'holes', the size of triangle edges must not exceed 0.7Δ (de Tullio & Pascazio 2016), thus implying that, for increasing Re_λ, not only the Eulerian mesh but also the Lagrangian triangulation must be refined to maintain the correct phase coupling. Accordingly, the values of N_l were 4912, 10048 or 21262, depending on the flow resolution.

995 A10-6

It is worth mentioning that N_p particles settling under their own weight impose on the fluid a force constantly aligned with gravity which, in a tri-periodic domain, would produce a continuous vertical acceleration of the flow and this would prevent the attainment of a statistical steady state. Following Chouippe & Uhlmann (2015), this is avoided by subtracting, at every time step, the mean of the IBM terms applied by the particles on the flow, thus imposing a force with zero average in all directions: this implies that the net momentum of the system must be on average zero. Thus, the downward motion of the falling particles is compensated by an upward motion of the fluid such as to give zero net vertical momentum (this is the analogue of the time-dependent pressure gradient in turbulent channel flows used to ensure a constant flow rate in time, Kim, Moin & Moser 1987). An analogous observation applies to angular momentum since free-falling chiral particles rotate in a preferred direction and this would generate a net circulation. In a tri-periodic cube, however, the Kelvin–Stokes theorem imposes zero circulation in all directions. Therefore, the angular velocity of particles is compensated by fluid vorticity in the opposite direction so as to maintain the circulation zero at every instant.

These observations must be kept in mind when analysing the results since while the resulting system can be efficiently simulated within homogeneous and isotropic conditions, an analogous laboratory experiment might not be immediately possible to set up.

2.5. *Particles*

The dynamics of the dispersed solid phase is obtained by solving, for each particle, the six degrees of freedom of the Newton–Euler equations:

$$
\left.
\begin{aligned}
&\left(\rho_p V_p \frac{\mathrm{d}\boldsymbol{u}_c}{\mathrm{d}t} = \oint_{A_p} \boldsymbol{\tau} \cdot \boldsymbol{n}\,\mathrm{d}A + (\rho_p - \rho_f)V_p \boldsymbol{g} + \boldsymbol{F}_c \right)^*, \\
&\left(\boldsymbol{I}_p \frac{\mathrm{d}\boldsymbol{\omega}_c}{\mathrm{d}t} + \boldsymbol{\omega}_c \times (\boldsymbol{I}_p \boldsymbol{\omega}_c) = \oint_{A_p} \boldsymbol{r} \times (\boldsymbol{\tau} \cdot \boldsymbol{n})\,\mathrm{d}A + \boldsymbol{T}_c \right)^*,
\end{aligned}
\right\}
\tag{2.6a,b}
$$

where the notation $(\cdot)^*$ implies a content in dimensional units. Here, A_p is the particle wet surface, $\boldsymbol{\tau} = -p\boldsymbol{I} + \mu_f(\nabla\boldsymbol{u} + \nabla\boldsymbol{u}^{\mathrm{T}})$ the Cauchy stress tensor for a Newtonian fluid with $\boldsymbol{I}$ the unit tensor, $\boldsymbol{n}$ is the outward normal of the particle surface and $\boldsymbol{I}_p$ the inertial tensor of the particle which, in the principal inertial reference frame (figure 1a), has only the diagonal components. Additionally, $\boldsymbol{F}_c$ and $\boldsymbol{T}_c$ represent respectively force and torque acting on the particle as result of collisions/physical contact with other particles.

Following Breugem (2012) and relying on Newton's third law of motion, we replace the integral terms on the right-hand side of (2.6a,b) with the volume forcing of the fluid phase, obtaining in non-dimensional form:

$$
\left.
\begin{aligned}
&\frac{\mathrm{d}\boldsymbol{u}_c}{\mathrm{d}t} \approx \frac{\rho_f}{\rho_p} \frac{6}{\pi} \left(-\sum_{i=1}^{N_l} \boldsymbol{f}_i \Delta V_i + \frac{\mathrm{d}}{\mathrm{d}t} \int_{V_p} \boldsymbol{u}\,\mathrm{d}V \right) - \frac{\hat{\boldsymbol{k}}}{Fr} + \frac{\rho_f}{\rho_p} \frac{6}{\pi} \boldsymbol{F}_c, \\
&\boldsymbol{I}_p \frac{\mathrm{d}\boldsymbol{\omega}_c}{\mathrm{d}t} + \boldsymbol{\omega}_c \times (\boldsymbol{I}_p \boldsymbol{\omega}_c) \approx \frac{\rho_f}{\rho_p} \frac{6}{\pi} \left(-\sum_{i=1}^{N_l} \boldsymbol{r}_i^n \times \boldsymbol{f}_i \Delta V_i + \frac{\mathrm{d}}{\mathrm{d}t} \int_{V_p} \boldsymbol{r} \times \boldsymbol{u}\,\mathrm{d}V \right) + \frac{\rho_f}{\rho_p} \frac{6}{\pi} \boldsymbol{T}_c,
\end{aligned}
\right\}
\tag{2.7}
$$

in which $\hat{\boldsymbol{k}}$ is the vertical unit vector and

$$Fr = \frac{U^2 \rho_p}{D_{eq}|\boldsymbol{g}|(\rho_p - \rho_f)} \qquad (2.8)$$

the Froude number. In the above expression, we note that surfaces are triangulated and each triangle is tagged by a Lagrangian marker at its centroid; thus, the index i indicates the Lagrangian point over the surface and ΔV_i is the volume of the Eulerian cell intersected.

It is important to note that (2.7) clearly shows the particle dynamics depend on two non-dimensional parameters, namely ρ_p/ρ_f and Fr, which in principle could be varied independently. Distinguishing between ρ_p/ρ_f and Fr, however, might look pleonastic since, in standard laboratory experiments within the same gravity field, ρ_p/ρ_f and Fr are not independent and (2.7) would in fact depend only on a single parameter. Accordingly, for the vast majority of our simulations, we have fixed the magnitude of gravity ($|\boldsymbol{g}| = 2$) and varied only ρ_p/ρ_f as an independent parameter. This value of $|\boldsymbol{g}|$ was initially selected since, for $\rho_p/\rho_f = 2$, it yielded $Fr = 1$.

However, centrifuge set-ups (Jiang *et al.* 2020) or microgravity environments (Futterer *et al.* 2013) could allow the independent variation of $\boldsymbol{g}$, thus making relevant studying the separate effect of Fr and ρ_p/ρ_f. In a few simulations, either of individual particles or of particle crowds, ρ_p/ρ_f and Fr have been varied independently, and a negligible effect of the former parameter compared with the latter has been observed; Appendix A reports some cases to confirm that indeed the results, for a fixed Froude number, hardly depend on density ratio variations.

The above model has been validated by considering a free-falling sphere in an initially quiescent viscous fluid. With a density ratio $\rho_p/\rho_f = 2$ ($Fr = 1$) and a fluid viscosity such to yield $Re \approx 1$ in the stationary state, the Stokes solution is expected to apply and this has been used for comparison. Domains up to $15 \times 15 \times 15$ in D_{eq} units with a resolution of 288^3 nodes have been employed and the results are given in figure 3(*a*) for the vertical velocity V and the drag force F_D; the agreement between the present data and the analytical Stokes solution for analogous quantities looks excellent, once the stationary state is attained. Similar calculations for the torque always yielded values within the round-off error as expected from the symmetry of the system geometry.

Unfortunately, exact results in the low-Re regime, as in figure 3(*a*), are not available for chiral particles. Therefore, we could only run consistency checks, showing opposite steady rotation for left- and right-handed particles. More in detail, starting from any initial orientation, a free-falling particle undergoes transient dynamics during which rotations occur about all three axes until the mass centroid attains the lowest possible position. Once this stable attitude is gained, only a constant rotation about the y_p (free-falling) axis remains which has opposite sign for different chirality of the particle (figure 3*b*). Additional simulations have revealed that the long-term dynamics is independent of the initial orientation which, instead, affects only the duration of the transient dynamics (figure 4); this has important consequences on the particle interaction with turbulence, which will be discussed in § 3. To further test this important finding, more simulations have been performed with decreased fluid viscosity so as to obtain a particle Reynolds number up to $Re_p = 260$. In another series of tests, the particle-to-fluid density ratio has been increased up to $\rho_p/\rho_f = 10$ obtaining a particle Reynolds number up to $Re_p = 555$. For all cases, even if within strongly unsteady fluctuations, similar dynamics as that described above has been observed thus confirming that the features are robust and mostly related to the specific particle geometry.
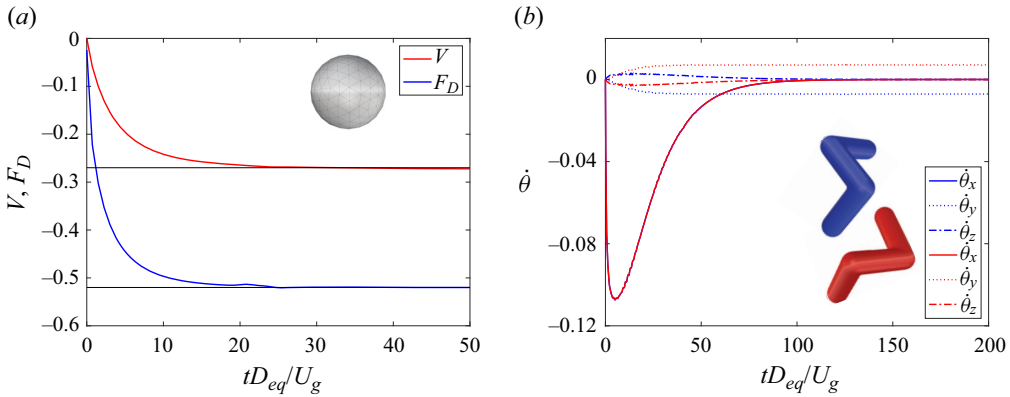
995 A10-8

Figure 3. Representative quantities for the Stokes dynamics of (*a*) a free-falling sphere and (*b*) chiral particles in a stagnant fluid. (*a*) Vertical velocity (red) and drag force (blue) are compared with the reference Stokes values (black). (*b*) Angular velocities in the body reference frame (green axes in figure 1) for a left-handed (blue) and right-handed (red) chiral particles. Note that here, since the external turbulence forcing is absent, the velocity scale U is undefined; all results are therefore scaled using $U_g = (|\rho_p/\rho_f - 1||\boldsymbol{g}|D_{eq})^{1/2}$.
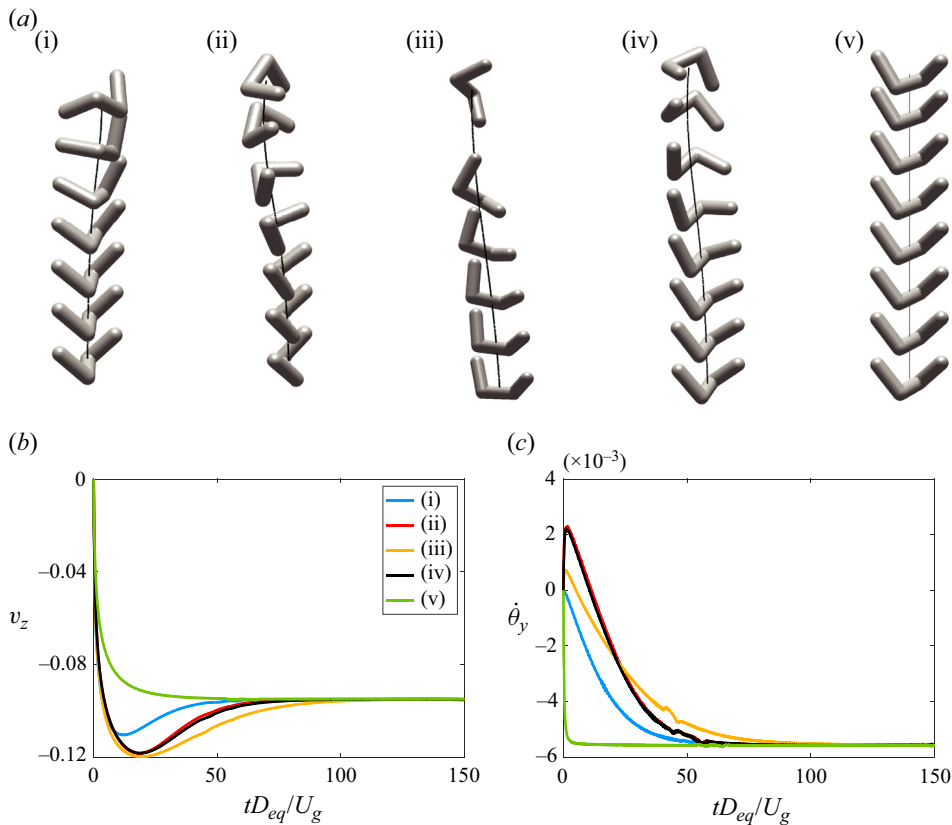
Figure 4. Initial transient dynamics of a chiral particle falling in a stagnant fluid, for different initial orientations, at $Re_p \approx 10$. The snapshots are taken at time lugs of $\Delta t D_{eq}/U_g = 10$. For the results of panels (*b*,*c*), the same scaling velocity as in figure 3 has been used.
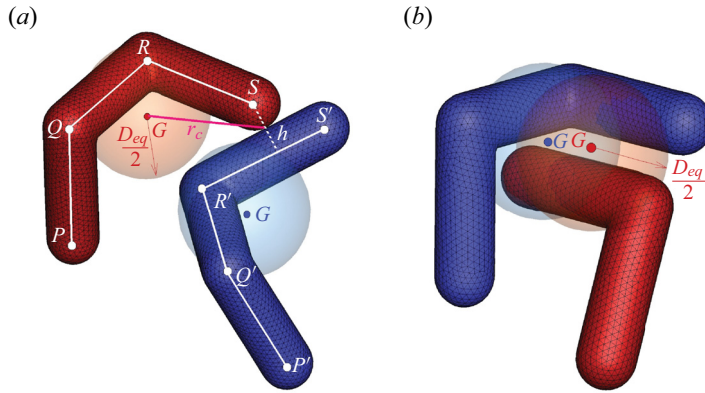
Figure 5. Possible configurations for close particles; the volume wise equivalent spheres are represented by transparent solids: (*a*) particles with a contact point but with non-intersecting spheres; (*b*) particles not in contact with intersecting spheres. The white segments in panel (*a*) are the axes of the particles legs used to compute proximity and contact.

An important aspect of the present problem is the evaluation of particle/particle collisions. In fact, we will see that, even if the volume fraction of the solid phase never exceeds $\phi = 2\%$, the complex shape of particles involves collisions with multiple contacts and even entanglement. Therefore, the correct interaction dynamics is relevant for the statistics of the whole system. Given the complex particle shape, determining interactions is not trivial as two bodies can have their centroids farther than D_{eq} even if there is contact (figure 5*a*) or *vice versa* (figure 5*b*).

In fact, the collision model consists of two main ingredients: the proximity detection and the contact loads computation. Concerning the former, each particle position and orientation is hard-coded through the coordinates of its nodal points P, Q, R and S (figure 5*a*), the diameter d of each leg (figure 1*a*), and the radius $d/2$ of each distal spherical cap. For any couple among the N_p particles, the centroids distance is computed and for those whose value is compatible with a contact, the minimum distance among the segments h is evaluated. Knowing the particle shape, it is easy to compute the thickness of the fluid gap between the two surfaces d_c and, if it is smaller than two Eulerian grid cells, the contact loads are computed. The reason for using $d_c \leq 2\Delta$ as the threshold value is that, in IBM methods, the flow at the first external point is not obtained from the Navier–Stokes equations but from a model which enforces the boundary conditions; if the gap between two immersed boundaries is thinner than 2Δ, only a single Eulerian point is available to satisfy two boundary conditions which is not a well-posed problem. Following Breugem (2012), the short-range repulsive force, which the *j*th particle exerts on the *i*th, is prescribed according to $\boldsymbol{F}_{c,ij} = -\alpha_c[(|\boldsymbol{d}_{ij}| - d_c)/d_c]^2 \boldsymbol{d}_{ij}/|\boldsymbol{d}_{ij}|$ with $\boldsymbol{d}_{ij}$ the oriented minimum surface distance during the collision. Here, $\alpha_c = 10^{-4}$ as in Breugem (2012) and $\boldsymbol{F}_{c,ji} = -\boldsymbol{F}_{c,ij}$ as prescribed by Newton's third law of motion. Finally, the contact force produces also a contact moment which is immediately computed from $\boldsymbol{T}_{c,ij} = \boldsymbol{r}_c \times \boldsymbol{F}_{c,ij}$, with $\boldsymbol{r}_c$ being the vector connecting the particle centroid with the contact point (figure 5*a*).

We refer to Assen *et al.* (2022) for additional details and a thorough validation of the collision model.
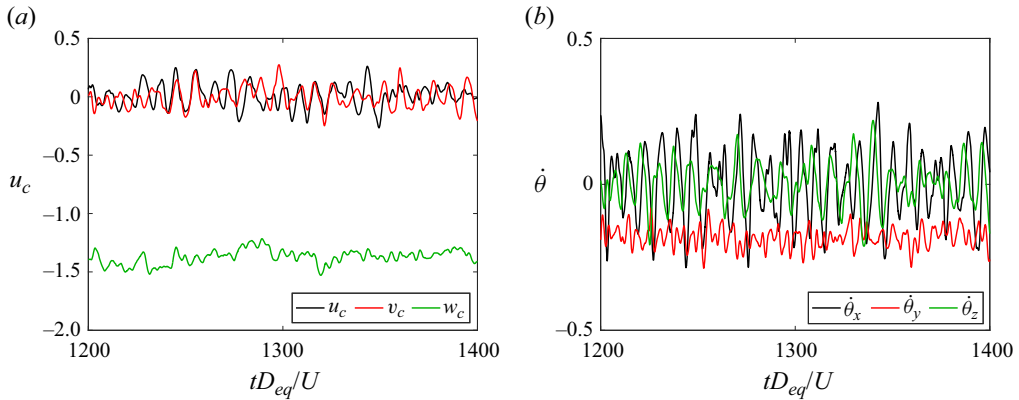
995 A10-10

Figure 6. Single chiral particle with $\rho_p/\rho_f = 2$ ($Fr = 1$) in a turbulent flow for the case Re15 of table 1. (*a*) Time evolution of the centre of mass velocity components. (*b*) Time evolution of angular velocity components expressed in the particle body frame (green axes in figure 1).

3. Results

3.1. *Turbulence intensity effect*

To understand how chiral bodies interact with the surrounding flow, we preliminarily consider the case of a single particle (volume fraction $\phi = 0.05\,\%$) in a turbulent environment of increasing intensity. We begin with a particle at $\rho_p/\rho_f = 2$ ($Fr = 1$) in weak turbulence, as for the case Re15 of table 1. Figure 6 shows also in this case a net rotation about the y_p body axis sustained by the vertical falling through the coupling of rotational and translational degrees of freedom.

Here, the dynamics does not differ much from that of figure 3(*b*), except for the unsteadiness whose origin is twofold: particle settling velocity and interaction with turbulence. In fact, $|\boldsymbol{u}_c|$ is proportional to $U_g = (|\rho_p/\rho_f - 1||\boldsymbol{g}|D_{eq})^{1/2}$, in turn setting the particle Reynolds number $Re_p = U_g D_{eq}/\nu$ and, for high enough values, this yields an unsteady falling even in a quiescent fluid (for the present flow parameters, it results in $Re_p \approx 140$). The interaction with turbulence, however, introduces further unsteadiness as the particle dynamics is coupled with velocity fluctuations whose strength is quantified by Re_λ. In this case, it results in $Re_\lambda \approx 14.7$ with a velocity ratio $u_{rms}/|v_z| \approx 0.08$, suggesting that turbulence acts only as a perturbation on the particle dynamics ($v_z = \boldsymbol{u}_c \cdot \hat{\boldsymbol{k}}$ is the falling particle velocity).

It is interesting to note that for the parameters of case Re15, single-phase turbulence yielded $Re_\lambda \approx 13$, while the introduction of a particle raises the value by more than 10 %; this is due to the constant energy injection caused by the particle free-fall (at the expense of its potential energy) which adds to the external forcing and increases the turbulence strength. Though the increase is small, the phenomenon underlines the two-way interaction between fluid and solid phases whose dynamics is strongly connected.

As Re_λ increases, the energy introduced by the particle becomes less relevant to turbulence while the stronger velocity fluctuations alter the solid body dynamics. In fact, for the parameters of case Re80, the effective Re_λ and u_{rms} are indistinguishable from the single-phase values while particle mean vertical and angular velocities become negligible when compared with their fluctuations.

The results are summarised in figure 7, which shows the mean vertical and angular velocities, both normalised by their standard deviations. It is worth pointing out that the
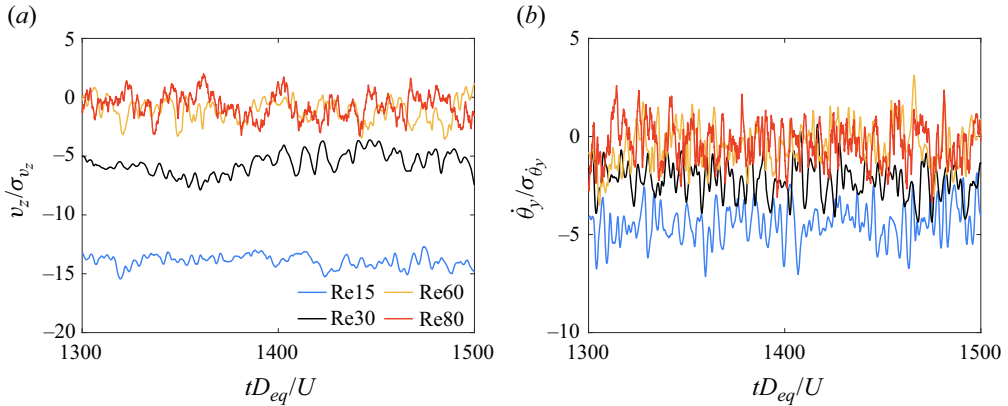
Figure 7. Single chiral particle with $\rho_p/\rho_f = 2$ ($Fr = 1$) in a turbulent flow for different turbulence strengths (see table 1). (*a*) Time evolution of the centre of mass vertical falling velocity. (*b*) Time evolution of the angular velocity about the y_p particle body axis (green axes in figure 1).
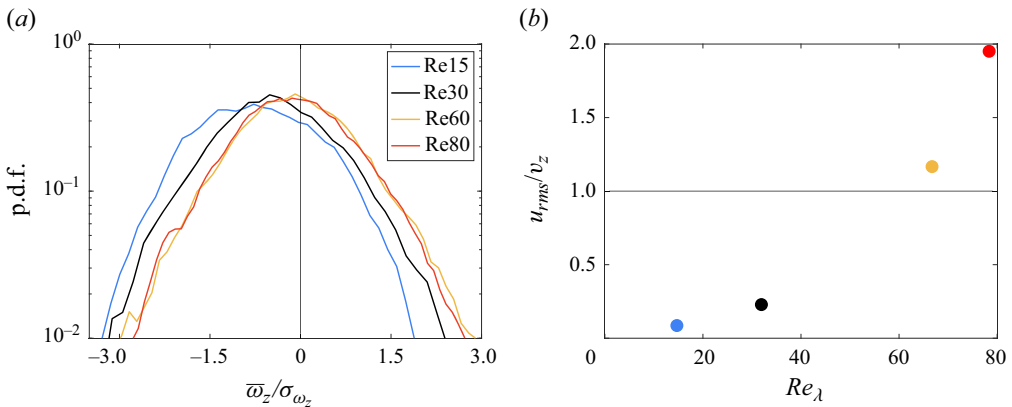

Figure 8. Single chiral particle with $\rho_p/\rho_f = 2$ ($Fr = 1$) in a turbulent flow at different Re_λ. (*a*) Probability density function of the fluid vertical vorticity component. A preferred vertical vorticity, due to the immersed chiral particles, is only obtained for weak turbulence. (*b*) Ratio of turbulent fluctuation intensity and mean vertical particle velocity as a function of the effective flow Re_λ.

ratio v_z/σ_{v_z} of figure 7(*a*) decreases with Re_λ, both because the standard deviation σ_{v_z} increases and because $|v_z|$ itself decreases. However, figure 7(*b*) shows that $|\dot\theta_y|$ remains approximately constant within this range of Re_λ although $\sigma_{\dot\theta_y}$ increases and therefore their ratio decreases.

An important effect of particle chirality is its mean angular velocity which, on account of the zero total circulation imposed by the domain boundary conditions, induces an opposite mean vorticity in the flow field. This is indeed observed from the probability density functions of the vertical fluid vorticity component (figure 8*a*) which are biased towards negative values and become more symmetric as Re_λ increases and particle rotation becomes less relevant.

These results are consistent with those of figure 7 suggesting that as turbulence strengthens, the particle tends to be passively advected by turbulent fluctuations rather than altering turbulence itself through its helical free-fall.
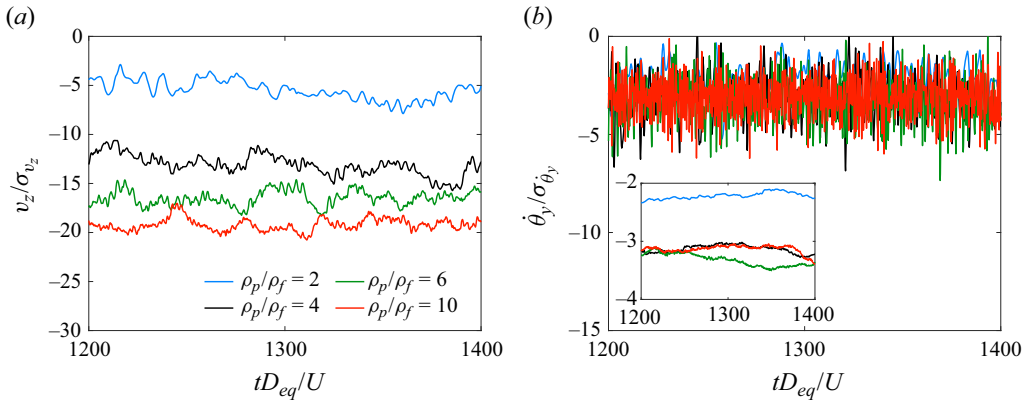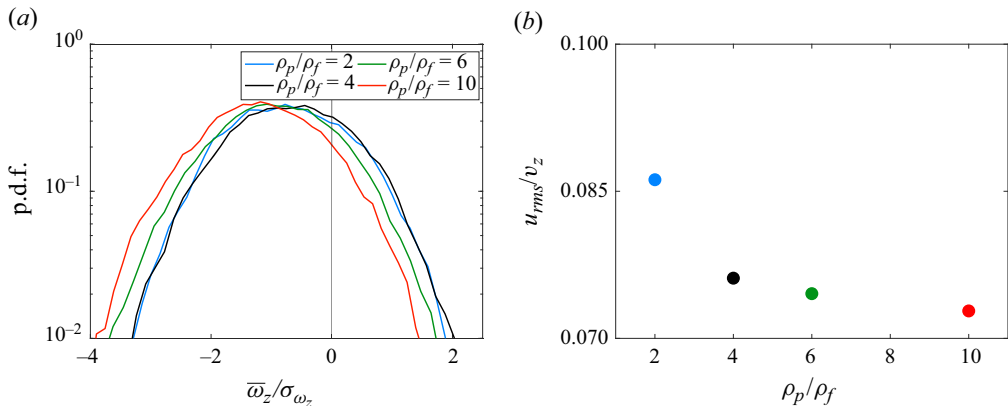
995 A10-12

Figure 9. Single chiral particle with ρ_p/ρ_f from 2 to 10 (*Fr* from 1 to 5/9) in a turbulent flow with the forcing of the Re15 case of table 1: (*a*) time evolution of the centre of mass velocity components; (*b*) time evolution of angular velocity components expressed in the particle body frame. In the inset, the same curves are plotted with a running average of $20D_{eq}/U$ time units to evidence their mean values.

A partial confirmation of this conjecture comes from figure 8(*b*), which reports the ratio between u_{rms} and $|v_z|$: when this ratio is small, particle dynamics dominates over turbulence which, therefore, is affected by particle chirality. In contrast, large Re_λ values result in $u_{rms}/|v_z| > 1$ and turbulent fluctuations dominate over particle forcing, yielding more isotropic dynamics.

3.2. *Density ratio effect*

Given the role played by the relative magnitude of turbulence fluctuations (u_{rms}) and the particle falling velocity $|v_z| \sim (|\rho_p/\rho_f - 1||\boldsymbol{g}|D_{eq})^{1/2}$, it should be clear that the system is sensitive not only to the strength of turbulence forcing but also to the density ratio ρ_p/ρ_f (or *Fr*). In fact, the immediate consequence of increasing ρ_p/ρ_f is to enhance the falling velocity and therefore the mean angular velocity. However, translation and rotation in a chiral particle are not rigidly coupled (as a nut and bolt assembly), as both depend on hydrodynamic loads. Therefore, they vary by different amounts. Moreover, the potential energy transfer of the falling particle grows with ρ_p/ρ_f, thus further increasing the turbulence level which reacts back on the particle dynamics. Finally, ρ_p/ρ_f changes particle inertia to translation and rotation, in turn altering the trajectory sensitivity to turbulent fluctuations.

Examples of particle dynamics are given in figure 9 where results at ρ_p/ρ_f from 2 to 10 (*Fr* $\in [1, 5/9]$) are compared for a turbulent forcing as the Re15 case of table 1: since for these flows, the interplay between mean values and standard deviations is more complex, we complement figure 9 with table 2 where additional data are provided. A clear trend can be observed for the mean vales of v_z and $\dot{\theta}_y$ which both increase in magnitude with the ratio ρ_p/ρ_f. Also, the effect of energy transfer, from particle to turbulence, is clearly evidenced from the growth of Re_λ and u_{rms}. A similar monotonic increase is found for the mean vertical component of the fluid vorticity which is a direct consequence of the chirality-induced angular velocity of the particle.

A closer look at the data, however, reveals that the fivefold increase of ρ_p/ρ_f produces growths of v_z of ≈ 3.6 and $\dot{\theta}_y$ of ≈ 2.7, thus confirming the loose coupling of particle rotation and translation. Concerning the effect on turbulence, $\overline{\omega}_z/\sigma_{\omega_z}$ grows by ≈ 1.6.

995 A10-13

ρ_p/ρ_f	$\langle v_z \rangle$	$\langle \dot{\theta}_y \rangle$	Re_λ	u_{rms}	$\overline{\omega}_z/\sigma_{\omega_z}$
2	−1.41	−0.17	14.7	0.12	−0.74
4	−2.80	−0.29	20.4	0.21	−0.67
6	−3.73	−0.36	23.4	0.28	−0.93
10	−5.16	−0.46	27.4	0.38	−1.17

Table 2. Flow parameters of single chiral particle simulations with variable ρ_p/ρ_f and turbulent forcing as the case Re15 of table 1.

Figure 10. Single chiral particle with ρ_p/ρ_f from 2 to 10 (*Fr* from 1 to 5/9) in a turbulent flow with the forcing of the Re15 case of table 1: (*a*) probability density function of the fluid vertical vorticity component; (*b*) ratio of turbulent fluctuation intensity and mean vertical particle velocity as function of ρ_p/ρ_f.

This is confirmed by the histograms of figure 10(*a*) which drift in the direction of negative vorticity consistently with the monotonic increase of $\dot{\theta}_y$. However, figure 10(*b*) shows how, despite the growth of Re_λ, the ratio $u_{rms}/|v_z|$ decreases with ρ_p/ρ_f, consistently with the observation that particles of larger density are less sensitive to turbulent fluctuations and their chirality makes them behave as impellers which impart rotation to the surrounding fluid.

We have repeated the same simulations as before, increasing the turbulence forcing as for the case Re30 of table 1. For the sake of conciseness, we report only the results of figure 11, which shows an effect of stronger turbulence only on the vorticity histograms of the lighter particles. Accordingly, the ratio u_{rms}/v_z shows a substantial increase for $\rho_p/\rho_f = 2$ and 4 (*Fr* = 1 and 2/3) while it is essentially unchanged for the higher density ratios.

The picture emerging from the simulations with a single chiral particle is that its fall injects additional energy in the fluid whose turbulence is altered; in turn, particle falling and rotational velocities are affected by the strength of velocity fluctuations. Therefore, the system dynamics emerges out of the balance of a complex two-way coupling between solid and fluid phases. Nevertheless, a clear trend is observed such that stronger velocity fluctuations reduce the effects of the particle and its chirality on turbulence, while higher particle/fluid density ratios increase them.
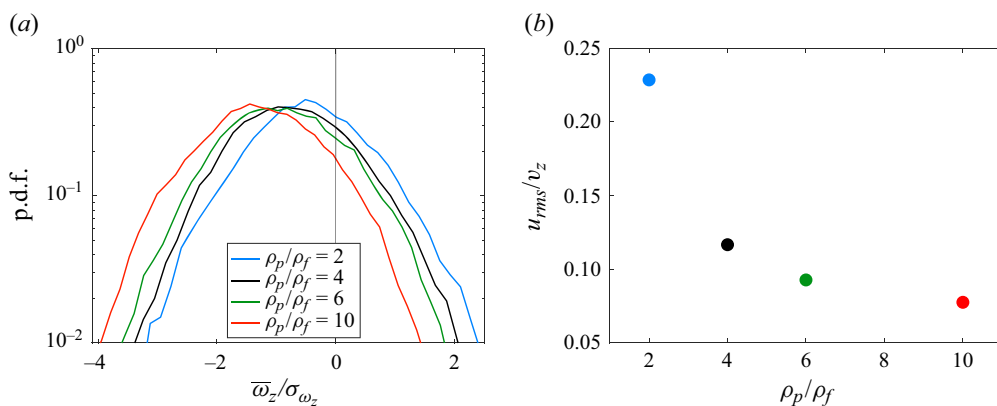
995 A10-14

Figure 11. Single chiral particle with ρ_p/ρ_f from 2 to 10 (Fr from 1 to 5/9) in a turbulent flow with the forcing of the Re30 case of table 1: (*a*) probability density function of the fluid vertical vorticity component; (*b*) ratio of turbulent fluctuation intensity and mean vertical particle velocity as a function of ρ_p/ρ_f. Note the very different vertical scale in figures 11(*b*) and 10(*b*).

3.3. *Volume fraction effect*

In real systems, such as helically swimming active matter (Liebchen & Levis 2022) or plants aiming at maximising seeds transport and dispersal (Mazzolai *et al.* 2021), multiple chiral particles interact simultaneously among them and react back on the surrounding fluid. Accordingly, we have investigated how the system dynamics changes when several particles are placed in a turbulent environment and what is the effect of their volume fraction ϕ.

The immediate effect of increasing the number of particles is to enhance the forcing on the turbulence, owing to growing energy injection in the fluid phase. However, the presence of multiple particles increases also energy dissipation, by friction with solid surfaces and the small scale of their wakes. Therefore, turbulence can be strengthened or suppressed, depending on which of the two mechanisms prevails.

Furthermore, the presence of obstacles in the bulk flow reduces the size attainable by the largest flow scales resulting in further modifications of the energy spectrum. Finally, the collision among complex shape particles favours prolonged interactions rather than impulsive rebounds, as in the case of spheres or other compact objects, and this changes the solid body dynamics and the interaction with the flow.

Table 3 reports some representative data for flows with a turbulent forcing as in the case Re30 of table 1 and an increasing number of particles with $\rho_p/\rho_f = 2$ ($Fr = 1$). It is indeed confirmed that a larger number of particles evolving within the same domain enhances velocity fluctuations, consistently with the augmented energy injection; however, viscous dissipation also increases and this happens at a faster rate than the increase of u_{rms}. The dependence of ε on ϕ is displayed in figure 12(*a*), which shows a linear behaviour which matches the findings of Fornari *et al.* (2019) for finite-size spheres in turbulence. The different growths of ε and u_{rms} with ϕ result in a decreasing Re_λ indicating that, for this set-up, more particles weaken turbulence by transferring more energy to small scales. This mechanism is quantitatively confirmed by the spectra of figure 12(*b*), which shows an increased energy content at the smallest scales and a reduced content at larger scales, which is similar to what was observed by Gao, Li & Wang (2013) in HIT flows with spheres of diameter $\approx \lambda$. The spectra of figure 12(*b*) also show that, for given ϕ, the present chiral particles are much more effective than spheres in modifying turbulence. This might be due

995 A10-15

N_p	ϕ (%)	$\langle v_z \rangle$	$\langle \dot\theta_y \rangle$	Re_λ	u_{rms}	ε	$\overline{\omega}_z/\sigma_{\omega_z}$
0	0	—	—	33.9	0.27	7.5×10^{-3}	0.00
1	0.05	−1.18	−0.17	31.9	0.27	8.0×10^{-3}	−0.43
5	0.25	−1.17	−0.17	29.5	0.29	1.2×10^{-2}	−0.86
10	0.50	−1.14	−0.17	28.1	0.30	1.6×10^{-2}	−1.21
20	1.00	−1.10	−0.16	24.4	0.31	2.5×10^{-2}	−1.59
40	2.00	−1.03	−0.16	22.9	0.34	4.0×10^{-2}	−1.67

Table 3. Flow parameters for multiple particle simulations with variable volume fraction ϕ, $\rho_p/\rho_f = 2$ ($Fr = 1$) and turbulent forcing as the case Re30 of table 1. Here, $\langle \rangle$ indicates an average over the particles.
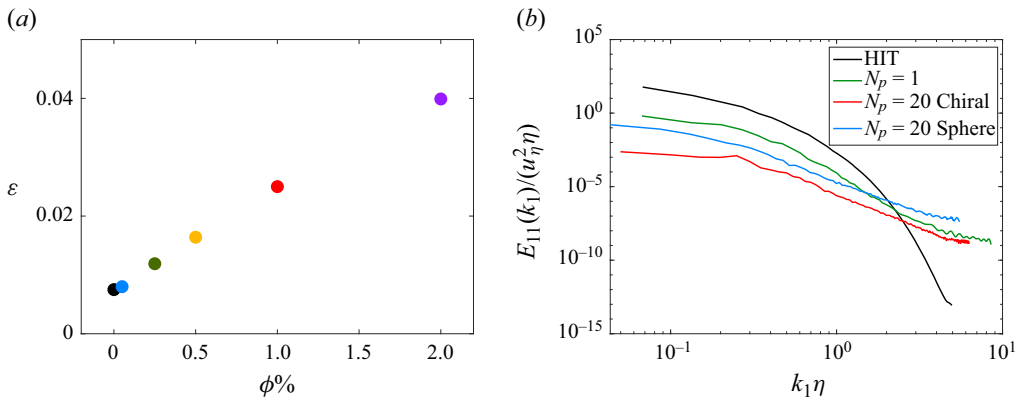
Figure 12. Multiple chiral particles with ϕ from 0.05 % to 2 % in a turbulent flow with the forcing the Re30 case of table 1 and $\rho_p/\rho_f = 2$: (*a*) kinetic energy dissipation rate as function of the volume fraction ϕ; (*b*) comparison of one-dimensional energy spectra for single-phase, one chiral particle, 20 chiral particles and 20 spheres.

to the angular momentum of the dispersed phase which in turn induces a net rotation of the fluid turbulence. Indeed, Biferale, Musacchio & Toschi (2013) have already shown that, in HIT, altering the nonlinear terms so as to have a sign-definite helicity content heavily affects the energy cascade and turbulence spectra.

A further consideration about the spectra of figure 12(*b*) is that, at first sight, it seems possible to collapse the spectra for spheres and chiral particles by a simple rescaling although several direct tests have shown that this is not the case. In fact, we would like to stress that chiral particles and spheres are equivalent only volume wise, while the wetted surface of the former is bigger by 50 % and the front area by 25 %. This implies that features like energy dissipation by friction and the surrounding fluid dragged during the motion cannot be accounted for by a single scaling factor.

An additional reason for the marked difference between spheres and chiral particles could be the collision dynamics, which is illustrated in figure 13. A set of N_p particles yields $N_p(N_p - 1)/2$ distinct couples, if pairs #*i*–#*j* and #*j*–#*i* are equivalent. Whenever particles #*i* and #*j* are close enough to activate the collision model, we assemble a four-digit integer #*ij* from the particles identification number, and record the time of interaction. Figure 13 shows, in a representative time window, the interactions for $N_p = 20$ spheres and chiral particles with the same volume fraction $\phi = 1\,\%$ for two flows with different
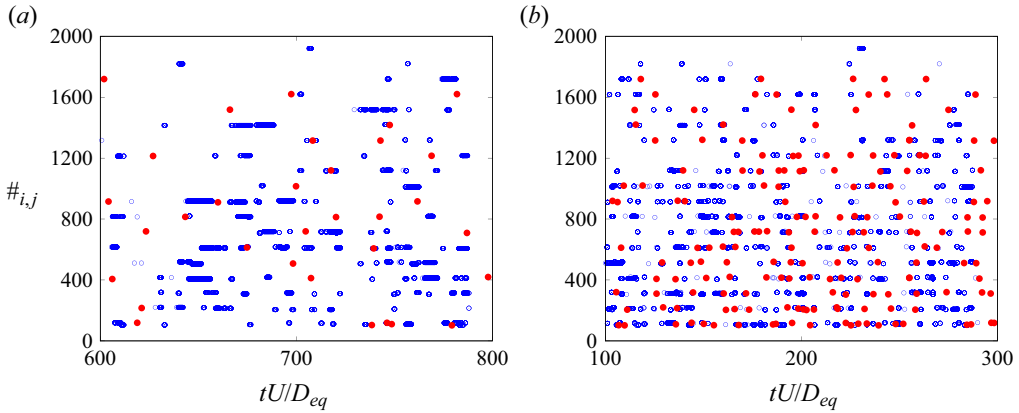
Figure 13. Collision events versus time for $N_p = 20$ particles ($\phi = 1\,\%$) in a turbulent flow: (*a*) forcing as the Re30 case of table 1 and $\rho_p/\rho_f = 2$; (*b*) forcing as the Re60 case of table 1 and $\rho_p/\rho_f = 7$; the four-digit number on the *y*-axis identifies the two interacting particles: for example, $\#i, j = 0412$ indicates that particles $\#i = 4$ and $\#j = 12$ have collided. Red bullets for spherical particles, blue open circles for chiral particles.

turbulent forcing and density ratios ρ_p/ρ_f. It is evident that spheres tend to have short duration impulsive rebounds, while chiral particles, with their complex shape, favour entanglement which entail multiple contacts over several time units. Analysis of the flow fields has evidenced an energy dissipation enhancement caused by particle collision which is consistent with the energy spectra of figure 12(*b*).

Clearly, frequency and duration of the collisions depend strongly on turbulence strength and particle density (figure 13). The comprehension of their statistics deserves a dedicated study which will be presented in a forthcoming paper.

Concerning the particle angular velocity, table 3 shows that it is essentially constant with ϕ, while the amplitude of the mean fluid vorticity increases (figure 14*a*); this can be explained by considering that $\langle \dot{\theta}_y \rangle$ is the mean angular velocity of each particle. When their number increases, the fluid must rotate faster to compensate for the total angular momentum which yields a global zero circulation.

The values of $\langle v_z \rangle$ slightly decrease with ϕ. This result agrees with the findings of Fornari, Picano & Brandt (2016) for spheres at similar volume fractions. The ratio $u_{rms}/\langle |v_z| \rangle$ is however well below unity for all volume fractions (figure 14*b*) and the vorticity histograms of figure 14(*a*) behave consistently, showing always asymmetric vorticity distributions.

After having investigated the effects of the single governing parameters separately, we can now vary them simultaneously and verify whether the system behaves according to the gained understanding. The picture emerging from the previous simulations is that particles fall because of gravity and increase turbulent fluctuations, by agitating the surrounding fluid at the expense of their potential energy. At the same time, also turbulent energy dissipation is enhanced. Thus, the overall turbulence strength (Re_λ) results from the balance of these two competing effects. However, particles settling velocity decreases as the turbulence strengthens, thus giving two-way coupled dynamics. The chiral shape of the present particles couples rotational and translational degrees of freedom which entails a net angular momentum of the solid phase and, correspondingly, a mean vorticity of the fluid turbulence. Finally, increasing the volume fractions ϕ of the chiral particles
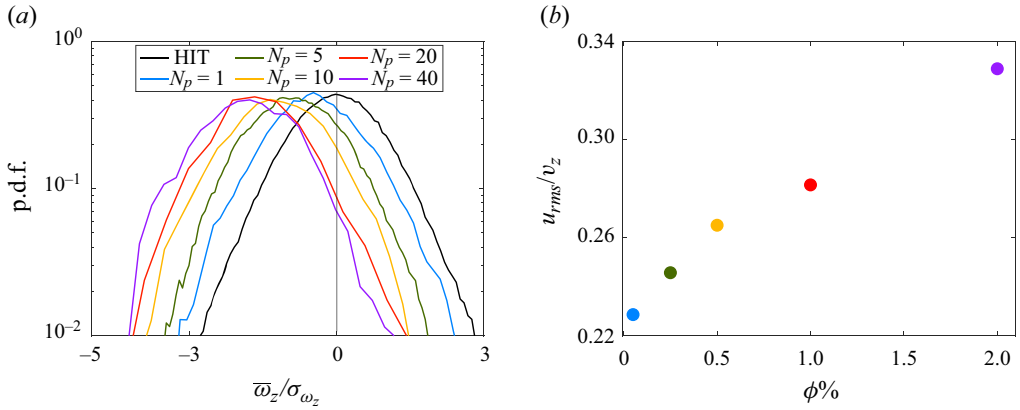
Figure 14. Multiple chiral particles with ϕ from 0.05 % to 2 % in a turbulent flow with the forcing of the Re30 case of table 1 and $\rho_p/\rho_f = 2$: (*a*) probability density function of the fluid vertical vorticity component; (*b*) ratio of turbulent fluctuation intensity and mean vertical particle velocity as a function of the volume fraction ϕ.
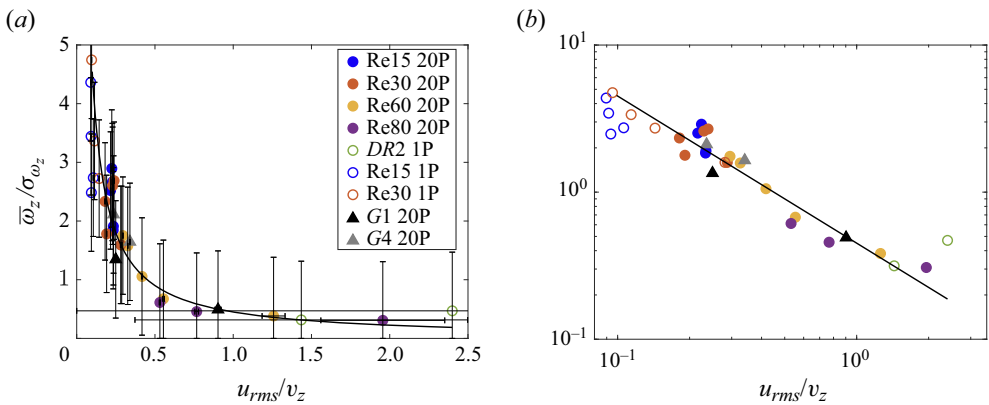

Figure 15. Mean flow vorticity normalised by its standard deviation versus ratio of turbulent velocity fluctuations with mean settling particle velocity in (*a*) linear and (*b*) logarithmic scale. The black solid line is the curve $0.45(u_{rms}/v_z)^{-1}$ which best fits all the simulations.

enhances the previous effects but introduces also a complex collision dynamics which further complicates the interactions.

On account of the above arguments, the relative strength of particle forcing and turbulence intensity can be quantified by the ratio $u_{rms}/\langle|v_z|\rangle$, while the chirality-induced flow rotation through the mean vorticity is normalised by its standard deviation $\langle\omega_z\rangle/\sigma_{\omega_z}$. Several simulation campaigns for different values of Re_λ and ρ_p/ρ_f have been performed. The results shown in figure 15 confirm that indeed the behaviour is well described by these quantities for a wide range of governing parameters. Some additional *ad hoc* cases have been run using different values of $\boldsymbol{g}$ to vary independently *Fr* and ρ_p/ρ_f: these data are also reported in figure 15. They collapse with the rest of the simulations in which only *Fr* has been varied as the main parameter.

It is important to note that most of the flows of figure 15 have been computed with $N_p = 20$ particles ($\phi = 1$ %) although we have verified that the same plot for all cases

995 A10-18

obtained using $N_p = 1$ ($\phi = 0.05\,\%$) behaves similarly even if data collapse onto a different curve. However, table 3 and the related discussion have evidenced that ϕ affects the flow features in several ways and parametrising its mechanisms is not trivial. However, we can attempt to estimate the effect of ϕ from table 3, which has been obtained for a single value of Re_λ and Fr, and verify whether the same correction works for all other flows. More in detail, from table 3, the quantities $u_{rms}/\langle|v_z|\rangle$ and $\langle\omega_z\rangle/\sigma_{\omega_z}$ at $N_p = 1$ and $N_p = 20$ have been employed to compute their ratios to be used as correction coefficients for all cases with $N_p = 1$ computed for different values of Re_λ and Fr. Indeed, the open symbols in figure 15 confirm that the behaviour is the same and all data now collapse on the same curve.

A final comment is concerning the huge error bar of the rightmost points in figure 15(*a*): in this case, the strength of turbulence (produced by the forcing f_T alone) is such as to make negligible the effect of the particle on the flow whose dynamics tends to that of a passive tracer. Accordingly, the settling velocity and the induced flow rotation should vanish while turbulent fluctuations strengthen. We have found that achieving statistical convergence for these cases requires very long simulation times (see also the large variations of the ratio T_o/T_e reported in § 2.1) and for $u_{rms}/\langle|v_z|\rangle > 2.5$, obtaining convergence becomes unpractical. We have however verified that, regardless of turbulence intensity, simulations with $\rho_p/\rho_f = 1$ always yield $\langle|v_z|\rangle \to 0$ and $\langle\omega_z\rangle \to 0$, thus confirming that the data of figure 15 approach the correct limit.

4. Conclusions and outlook

Using direct numerical simulations of homogeneous isotropic turbulence with finite–size, heavy chiral particles, we have investigated the dynamics of the system under the influence of the main governing parameters which are: turbulence strength, solid-to-fluid density ratio (or Froude number) and volume fraction of the solid phase.

A particle, falling under the effect of an external gravity field, converts its potential energy into a kinetic counterpart which is transferred to the fluid through viscous and pressure forces. On the one hand, this mechanism enhances the intensity of velocity fluctuations but, on the other hand, it also increases the energy dissipation through viscous friction and the generation of small scales in the wake. Depending on the specific flow parameters, the former or the latter mechanisms can prevail, thus boosting or suppressing turbulence intensity, respectively.

Turbulence of increasing strength, in turn, affects particle dynamics by reducing its mean falling velocity and decreasing the relevance of the additional energy input with respect to that introduced by the HIT forcing alone.

Particle chirality, by coupling translational and rotational degrees of freedom, produces a mean flow vorticity which is evidenced through its probability density function with a non-zero peak position.

Our results suggest that the ratio of turbulent velocity fluctuations to the mean particle settling velocity u_{rms}/v_z can be used to characterise the intensity of the chirality induced mean rotation of the flow which decreases as the previous ratio increases: the implication of this finding is that particle chirality does not matter much in large-scale features of strong turbulence.

The influence of the particle volume fraction ϕ is more complex than the other parameters since, in addition to the above-mentioned mechanisms, there are the interactions among particles and their collisions. The latter have shown to be characterised by long entanglement times in contrast to spheres which instead rebound impulsively. These differences are evident also from the turbulent energy spectra which, for a given

volume fraction ($\phi = 1\,\%$), show a more pronounced energy reduction caused by chiral particles than by spheres. Despite the more complex dynamics, the quantity u_{rms}/v_z describes correctly the induced flow rotation as confirmed by figure 15.

This paper is only a first attempt to investigate the interaction of relatively complex shaped chiral particles with homogeneous isotropic turbulence and many things could be done to extend the study in different ways: more detailed flow statistics should be computed to understand how turbulence is modified not only with respect to rotation. Although the work done by the falling particles may be negligible for altering the energetics of larger scales in the flow, it could be significant at smaller scales. At these scales where the energy injection due to the particles is significant, the particle chirality might also matter. An extreme case confirming this observation is that for 50 % mixtures of left- and right-handed particles, flow vorticity does not change although the small-scale features of turbulence is altered.

Heavier and lighter spheres in HIT (such as droplets in gases and droplets in liquids, respectively), owing to centrifugal effects, are known to collect in different flow regions. Thus, chiral particles lighter than the surrounding fluid might behave differently from the present ones. In this paper, we have verified that left- and right-handed particles behave identically except for the sign of the induced flow rotation. A 50 % mixture of left- and right-handed particles is expected to produce zero net rotation of the flow although it is likely to alter other turbulence properties very differently from a set of spheres with the same ϕ. Finally, the statistics of particle collisions has shown to strongly depend on the various flow parameters (figure 13). A deeper understanding of their features would be very useful to characterise the dynamics of real suspensions.

All these points are currently under investigation or will be dealt with in the near future. They will be the subject of forthcoming papers.

Declaration of interests. The authors report no conflict of interest.

Data availability statement. The data that support the findings of this study are available upon reasonable request.

Author ORCIDs.

Ⓓ G. Piumini https://orcid.org/0009-0002-4463-6257;

Ⓓ M.P.A. Assen https://orcid.org/0000-0002-8054-6198;

Ⓓ D. Lohse https://orcid.org/0000-0003-4138-2255;

Ⓓ R. Verzicco https://orcid.org/0000-0002-2690-9998.

Appendix A. Density ratio independence if $Fr = 1$

In this appendix, we provide evidence of the reduced sensitivity of (2.7) to density ratio compared with the Froude number. Figure 16 reports some cases run for $2 \leq \rho_p/\rho_f \leq 20$ and $Fr = 1$, showing only limited differences. Indeed, some effects are evident for the settling velocity, especially for the lowest density ratio. These however have to be
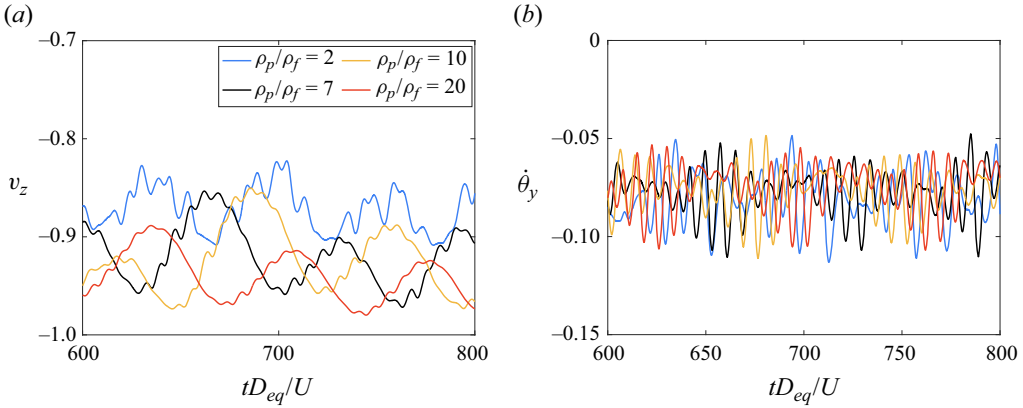
(*a*)

(*b*)

Figure 16. Single chiral particle falling in a stagnant fluid at $Re_p \approx 100$ for different ρ_p/ρ_f and fixed $Fr = 1$. (*a*) Time evolution of the centre of mass vertical velocity component. (*b*) Time evolution of angular velocity *y*-component expressed in the particle body frame (green axes in figure 1).

compared with the results of figure 9 where a smaller variation of *Fr* produces much larger effects.

As an aside, we note that if $U_g = \sqrt{D(\rho_f/\rho_p - 1)|\boldsymbol{g}|}$ is used as scaling velocity for all equations (rather than the flow velocity U), the Froude number turns out to be always $Fr = 1$ and the resulting system shows only limited sensitivity to the density ratio ρ_p/ρ_f.

Appendix B. Kinetic energy balance

As a further consistency check of the numerics, we consider the energy budget obtained from (2.1*a,b*) after a scalar product with $\boldsymbol{u}$ and integrating over the entire domain Ω. We obtain, for the kinetic energy $E_k = \boldsymbol{u} \cdot \boldsymbol{u}/2$, the following relation:

$$\frac{\mathrm{d}}{\mathrm{d}t}\langle E_k \rangle_\Omega = -\varepsilon_\Omega + \Pi_T + \Pi_P \tag{B1}$$

with the dissipation rate

$$\varepsilon_\Omega = \frac{1}{Re}\left\langle \left|\frac{\partial \boldsymbol{u}}{\partial \boldsymbol{x}}\right|^2 \right\rangle_\Omega, \tag{B2}$$

the work done by the turbulence forcing Π_T,

$$\Pi_T = \langle \boldsymbol{u} \cdot \boldsymbol{f}_T \rangle_\Omega, \tag{B3}$$

and the fluid–particle coupling term Π_P,

$$\Pi_P = \langle \boldsymbol{u} \cdot \boldsymbol{f}_P \rangle_\Omega. \tag{B4}$$

Figure 17 shows the time evolution of the left- and right-hand side of (B1), confirming the balance.

Appendix C. Computational domain size in gravity direction

Here we provide the results of additional simulations run in a computational domain whose size has been doubled in the gravity direction ($L_z = 20D_{eq}$). These tests were
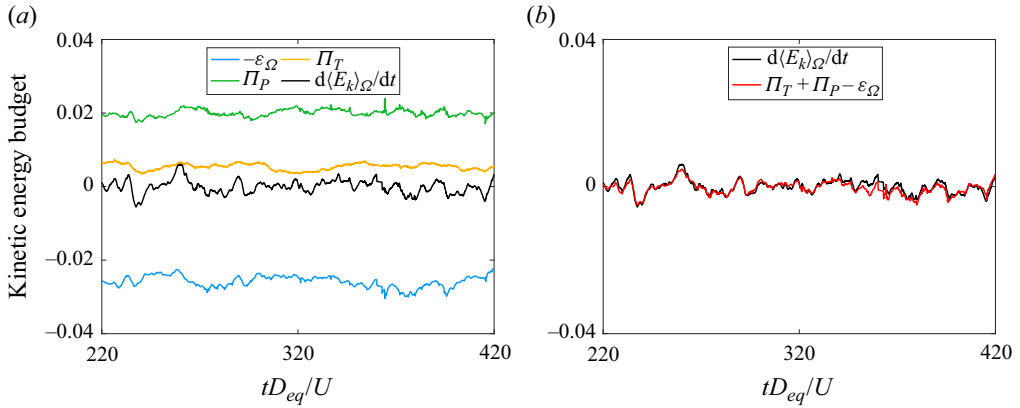
(*a*)

(*b*)

Figure 17. Time evolution of left- and right-hand side of (B1) for $N_p = 20$ chiral particles of $\rho_p/\rho_f = 2$ in the forcing case Re30 of table 1. The right-hand side terms are shown both (*a*) individually and (*b*) in sum.
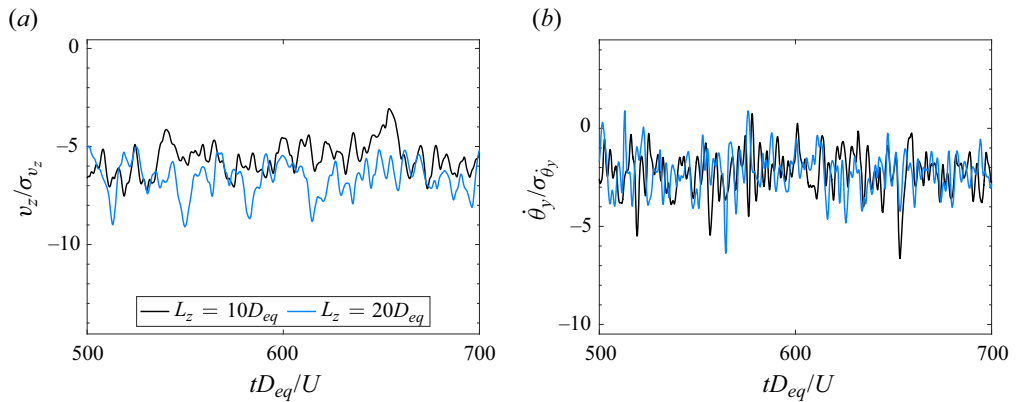
(*a*)

(*b*)

Figure 18. Single chiral particle of $\rho_p/\rho_f = 2$ in a turbulent flow with the forcing of the Re30 case of table 1: (*a*) time evolution of the centre of mass vertical velocity component; (*b*) time evolution of angular velocity y-component expressed in the particle body frame (green axes in figure 1).

run to ascertain a possible influence of the vertical domain size on account of particles settling velocity. Figure 18 shows the time evolution settling and angular velocity for a single particle at $\rho_p/\rho_f = 2$ in a turbulent flow with the forcing as the case Re30 of table 1: their mean values are $v_z/\sigma_{v_z} = -6.7 \pm 1.0$, -2.3 ± 0.3 for $L_z = 20D_{eq}$ and $v_z/\sigma_{v_z} = -5.8 \pm 1.1$, -2.1 ± 0.3 for $L_z = 10D_{eq}$, thus confirming that the cubic domain is indeed adequate for our analyses.

In figure 19, we report the results of a similar test performed for a crowd of particles at $\rho_p/\rho_f = 2$ in a turbulent flow with the forcing as the case Re30 of table 1 and $\phi = 1\%$ ($N_p = 40$); once again the results show very good agreement with the analogous ones obtained in a cubic computational domain.
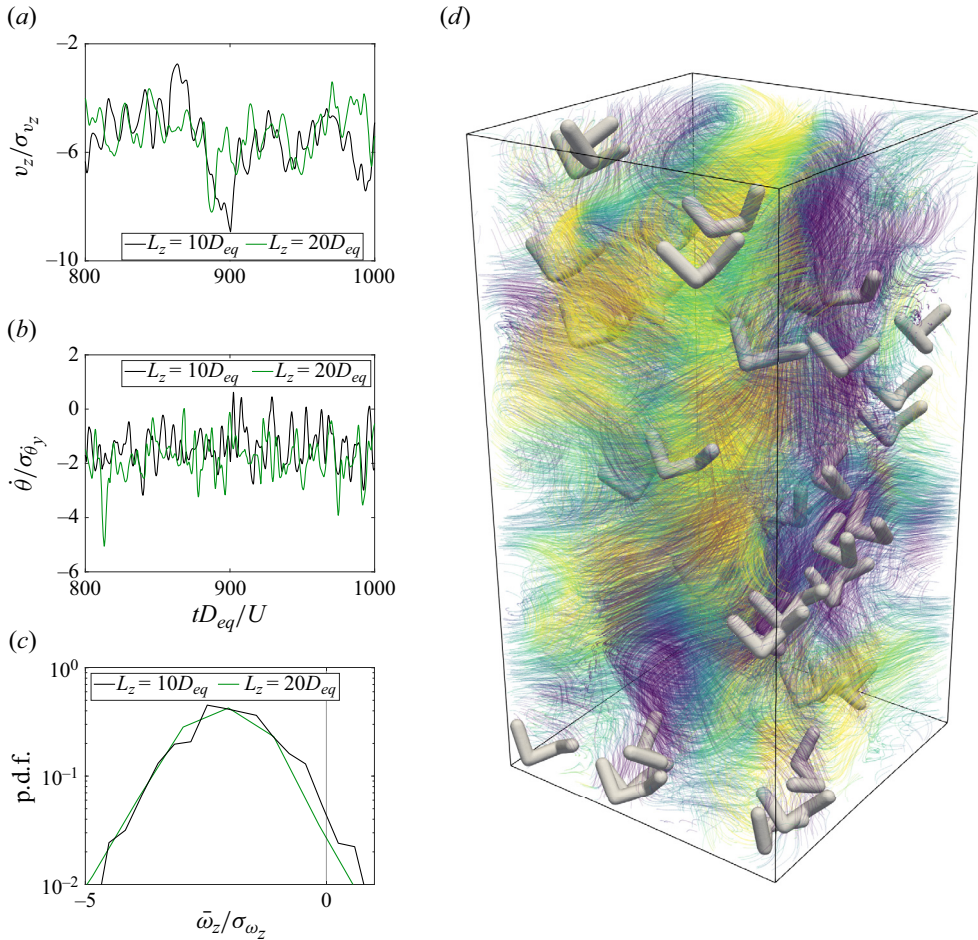
995 A10-22

Figure 19. Crowd of chiral particles of $\rho_p/\rho_f = 2$ in a turbulent flow with the forcing of the Re30 case of table 1: (*a*) time evolution of the centre of mass vertical velocity component; (*b*) time evolution of angular velocity *y*-component expressed in the particle body frame (green lines in figure 1); (*c*) probability density function of the fluid vertical vorticity component; (*d*) streamlines of the non-dimensional velocity field coloured according to the vertical component ranging from -0.3 (blue) to 0.3 (yellow).

REFERENCES

ASSEN, M.P.A., NG, C.S., WILL, J.B., STEVENS, R.J.A.M., LOHSE, D. & VERZICCO, R. 2022 Strong alignment of prolate ellipsoids in Taylor–Couette flow. *J. Fluid Mech.* **935**, A7.

BALMFORTH, N. & PROVENZALE, A. 2001 *Geomorphological Fluid Mechanics*, 1st edn. Springer.

BEC, J., GUSTAVSSON, K. & MEHLIG, B. 2024 Statistical models for the dynamics of heavy particles in turbulence. *Annu. Rev. Fluid Mech.* **56** (1), 189–213.

BIFERALE, L., MUSACCHIO, S. & TOSCHI, F. 2013 Split energy-helicity cascades in three-dimensional homogeneous and isotropic turbulence. *J. Fluid Mech.* **730**, 309–327.

BRANDT, L. & COLETTI, F. 2022 Particle-laden turbulence: progress and perspectives. *Annu. Rev. Fluid Mech.* **54** (1), 159–189.

BREUGEM, W.-P. 2012 A second-order accurate immersed boundary method for fully resolved simulations of particle-laden flows. *J. Comput. Phys.* **231** (13), 4469–4498.

CHAN, C.W., WU, D., QIAO, K., FONG, K.L., YANG, Z., HAN, Y. & ZHANG, R. 2024 Chiral active particles are sensitive reporters to environmental geometry. *Nat. Commun.* **15** (1).

CHOUIPPE, A. & UHLMANN, M. 2015 Forcing homogeneous turbulence in direct numerical simulation of particulate flow with interface resolution and gravity. *Phys. Fluids* **27** (12), 123301.

DI GIUSTO, D. & MARCHIOLI, C. 2022 Turbulence modulation by slender fibers. *Fluids* **7**, 255.

DOTTO, L. & MARCHIOLI, C. 2019 Orientation, distribution, and deformation of inertial flexible fibers in turbulent channel flow. *Acta Mechanica* **230**, 597–621.

ESWARAN, V. & POPE, S.B. 1988 An examination of forcing in direct numerical simulations of turbulence. *Comput. Fluids* **16** (3), 257–278.

FORNARI, W., PICANO, F. & BRANDT, L. 2016 Sedimentation of finite-size spheres in quiescent and turbulent environments. *J. Fluid Mech.* **788**, 640–669.

FORNARI, W., ZADE, S., BRANDT, L. & PICANO, F. 2019 Settling of finite-size particles in turbulence at different volume fractions. *Acta Mechanica* **230**, 413–430.

FUTTERER, B., KREBS, A., PLESA, A.-C., ZAUSSINGER, F., HOLLERBACH, R., BREUER, D. & EGBERS, C. 2013 Sheet-like and plume-like thermal flow in a spherical convection experiment performed under microgravity. *J. Fluid Mech.* **735**, 647–683.

GAO, H., LI, H. & WANG, L.-P. 2013 Lattice Boltzmann simulation of turbulent flow laden with finite-size particles. *Comput. Maths Applics.* **65**, 194–210.

HARGRAVE, B.T. 1985 Particle sedimentation in the ocean. *Ecol. Modell.* **30** (3), 229–246.

JIANG, H., ZU, X., WANG, D., HUISMAN, S.G. & SUN, C. 2020 Supergravitational turbulent thermal convection. *Sci. Adv.* **6**, eabb8676.

JIMÉNEZ, J., WRAY, A., SAFFMAN, P.G. & ROGALLO, R.S. 1993 The structure of intense vorticity in isotropic turbulence. *J. Fluid Mech.* **255**, 65–90.

KIM, J., MOIN, P. & MOSER, R. 1987 Turbulence statistics in fully developed channel flow at low Reynolds number. *J. Fluid Mech.* **177**, 133–166.

LASHGARI, I., PICANO, F., BREUGEM, W.-P. & BRANDT, L. 2014 Laminar, turbulent, and inertial shear-thickening regimes in channel flow of neutrally buoyant particle suspensions. *Phys. Rev. Lett.* **113**, 254502.

LIEBCHEN, B. & LEVIS, D. 2022 Chiral active matter. *Europhys. Lett.* **65**, 67001.

MAZZOLAI, B., MARIANI, S., RONZAN, M., CECCHINI, L., FIORELLO, I., CIKALLESHI, K. & MARGHERI, L. 2021 Morphological computation in plant seeds for a new generation of self-burial and flying soft robots. *Frontiers* **8**.

NECKER, F., HÄRTEL, C., KLEISER, L. & MEIBURG, E. 2005 Mixing and dissipation in particle-driven gravity currents. *J. Fluid Mech.* **545**, 339–372.

OLIVIERI, S., CANNON, I. & ROSTI, M.E. 2022 The effect of particle anisotropy on the modulation of turbulent flows. *J. Fluid Mech.* **950**, R2.

VAN DER POEL, E.P., OSTILLA-MÓNICO, R., DONNERS, J. & VERZICCO, R. 2015 A pencil distributed finite difference code for strongly turbulent wall-bounded flows. *Comput. Fluids* **116**, 10–16.

RAI, M.M. & MOIN, P. 1991 Direct simulations of turbulent flow using finite-difference schemes. *J. Comput. Phys.* **96** (1), 15–53.

ROGALLO, R.S. 1981 Numerical experiments in homogeneous turbulence. NASA TM-81315 https://ntrs.nasa.gov/citations/19810022965.

ROMA, A.M., PESKIN, C.S. & BERGER, M.J. 1999 An adaptive version of the immersed boundary method. *J. Comput. Phys.* **153** (2), 509–534.

ROOS, G. & ROOS, C. 2015 Chapter 3 - Isomers and stereochemistry. In *Organic Chemistry Concepts* (ed. G. Roos & C. Roos), pp. 43–54. Academic Press.

SHAW, R.A. 2003 Particle-turbulence interactions in atmospheric clouds. *Annu. Rev. Fluid Mech.* **35** (1), 183–227.

SOZZA, A., CENCINI, M., MUSACCHIO, S. & BOFFETTA, G. 2022 Instability of a dusty Kolmogorov flow. *J. Fluid Mech.* **931**, A26.

SPANDAN, V., PUTT, D., OSTILLA-MÓNICO, R. & LEE, A.A. 2020 Fluctuation-induced force in homogeneous isotropic turbulence. *Sci. Adv.* **6**, eaba0461.

TOSCHI, F. & BODENSCHATZ, E. 2009 Lagrangian properties of particles in turbulence. *Annu. Rev. Fluid Mech.* **41** (1), 375–404.

DE TULLIO, M.D. & PASCAZIO, G. 2016 A moving-least-squares immersed boundary method for simulating the fluid–structure interaction of elastic bodies with arbitrary thickness. *J. Comput. Phys.* **325**, 201–225.

VERZICCO, R. & ORLANDI, P. 1996 A finite-difference scheme for three-dimensional incompressible flows in cylindrical coordinates. *J. Comput. Phys.* **123** (2), 402–414.

VOILLAND, A. 2018 Here comes the saharan dust. https://earthobservatory.nasa.gov/images/92358/here-comes-the-saharan-dust.

VOTH, G.A. & SOLDATI, A. 2017 Anisotropic particles in turbulence. *Annu. Rev. Fluid Mech.* **49** (1), 249–276.

YU, Z., XIA, Y., GUO, Y. & LIN, J. 2021 Modulation of turbulence intensity by heavy finite-size particles in upward channel flow. *J. Fluid Mech.* **913**, A3.

ZHAO, L.H., ANDERSSON, H.I. & GILLISSEN, J.J.J. 2010 Turbulence modulation and drag reduction by spherical particles. *Phys. Fluids* **22** (8), 081702.